J. Fluid Mech. (1997), *vol.* 342, *pp.* 179–197. Printed in the United Kingdom

Instabilities of fully developed rapid flow of a granular material in a channel

By CHI-HWA WANG†, R. JACKSON AND S. SUNDARESAN
Department of Chemical Engineering, Princeton University, Princeton, NJ 05844-5263, USA

(Received 27 July 1996 and in revised form 18 February 1997)

The equations of motion for 'rapid' flow of a granular material have fully developed solutions representing flow driven by a body force, such as gravity, along a channel bounded by plane parallel walls. The stability of these solutions to small perturbations is investigated. For given properties of the particles and the channel walls it is found that the condition of critical stability is a relation between the mean concentration of the particles and the width of the channel. When the base state is unstable the fastest growing modes are travelling waves propagating in the axial direction and these induce characteristic patterns of variations in particle concentration, as well as velocity. These instabilities are contrasted with those found for Couette shearing in an earlier publication.

1. Introduction

In a previous paper (Wang, Jackson & Sundaresan 1996) we investigated the stability of a layer of granular material sheared rapidly between parallel solid plates, in the absence of gravity. This appears to be the first treatment of stability of a bounded flow for granular materials, though several earlier publications addressed the stability of an unbounded uniformly shearing material (Savage 1992; Babić 1993*a*; Schmid & Kytomaa 1994) and direct dynamic simulations show clear indications of unstable behaviour (Hopkins & Louge 1991; Goldhirsch, Tan & Zanetti 1993). The relation between this work and our results on bounded shear is discussed in detail in our previous paper (Wang *et al.* 1996).

In this paper we turn attention to the stability of a fully developed convective flow of granular material along a channel bounded by parallel plane walls. The flow is induced by a body force, for example gravity, directed along the channel. The equations of motion and the boundary conditions are the same as those used in our treatment of the bounded shear layer, but the instabilities found are of a distinctly different nature.

2. Governing equations

Figure 1 shows the configuration to be studied and illustrates some notation. Cartesian coordinates are set up with the x-axis vertical and the y-axis normal to the boundaries of the channel, which is assumed to be infinite in extent in the z-direction. The boundaries are vertical and are separated by a distance Δ, and the base state is one of fully developed flow downward under gravity. In this state the normal force per unit area exerted on the boundaries by the granular material is denoted by N.

† Present address: Department of Chemical Engineering, National University of Singapore.

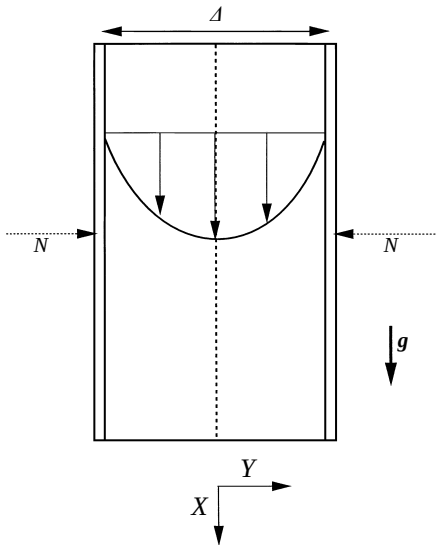

FIGURE 1. Flow in a vertical channel. N = normal stress on channel walls, $\boldsymbol{g}$ = specific gravity force.

The equations of motion are those used in Wang *et al.* (1996), augmented by a gravitational force in the x-direction, namely

$$\frac{\partial \rho}{\partial t} + \boldsymbol{\nabla}\cdot(\rho \boldsymbol{u}) = 0, \tag{1}$$

$$\rho \frac{\mathrm{D}\boldsymbol{u}}{\mathrm{D}t} = -\boldsymbol{\nabla}\cdot\boldsymbol{\sigma} + \rho \boldsymbol{g}, \tag{2}$$

$$\tfrac{3}{2}\rho \frac{\mathrm{D}T}{\mathrm{D}t} = -\boldsymbol{\nabla}\cdot\boldsymbol{q} - \boldsymbol{\sigma}\colon\boldsymbol{\nabla}\boldsymbol{u} - J. \tag{3}$$

Here $\boldsymbol{g}$ is the specific gravity force vector, ρ is the bulk density of the material, given by $\rho = \rho_p \nu$, where ν is the volume fraction of solids and ρ_p the density of the solid material; $\boldsymbol{u}$ is the local mean velocity, $\boldsymbol{\sigma}$ is the stress tensor for the granular assembly and T is the grain temperature, defined as $\frac{1}{3}\langle u'^2\rangle$, where u' is the magnitude of the fluctuation about the local mean velocity; $\boldsymbol{q}$ is the flux vector of the pseudo-thermal energy associated with the fluctuations in particle velocity, and J denotes the rate of dissipation of this energy, per unit volume, by inelastic collisions between particles. $\mathrm{D}/\mathrm{D}t$ represents the material time derivative following the mean motion.

The closures adopted for $\boldsymbol{\sigma}$, $\boldsymbol{q}$ and J are those of Lun *et al.* (1984), namely

$$\boldsymbol{\sigma} = [\rho T(1+4\eta\nu g_0) - \eta\mu_b \boldsymbol{\nabla}\cdot\boldsymbol{u}]\boldsymbol{I} - \left(\frac{2+\alpha}{3}\right)\left\{\frac{2\mu}{\eta(2-\eta)g_0}\left(1+\frac{8}{5}\nu\eta g_0\right)\left[1+\frac{8}{5}\eta(3\eta-2)\nu g_0\right] + \frac{6}{5}\eta\mu_b\right\}\boldsymbol{S}, \tag{4}$$

$$\boldsymbol{q} = -\frac{\lambda}{g_0}\left\{\left(1+\frac{12}{5}\eta\nu g_0\right)\left[1+\frac{12}{5}\eta^2(4\eta-3)\nu g_0\right] + \frac{64}{25\pi}(41-33\eta)(\eta\nu g_0)^2\right\}\boldsymbol{\nabla}T - \frac{\lambda}{g_0}\frac{12}{5}\eta(\eta-1)(2\eta-1)\left[1+\frac{12}{5}\eta\nu g_0\right]\frac{\mathrm{d}}{\mathrm{d}\nu}(\nu^2 g_0)\frac{T}{\nu}\boldsymbol{\nabla}\nu, \tag{5}$$

$$J = \frac{48}{\pi^{1/2}}\eta(1-\eta)\frac{\rho_p \nu^2}{d} g_0 T^{3/2}, \tag{6}$$

where $\boldsymbol{S}$ is the deviatoric part of the rate of deformation:

$$\boldsymbol{S} = \tfrac{1}{2}(\boldsymbol{\nabla u} + \boldsymbol{\nabla u}^T) - \tfrac{1}{3}\boldsymbol{\nabla \cdot u I};$$

$\eta = \frac{1}{2}(1+e_p)$, where e_p is the coefficient of restitution for collisions between particles; while two viscosity factors μ and μ_b, and the thermal conductivity factor λ, are given by

$$\mu = \frac{5M(T/\pi)^{1/2}}{16d^2}; \quad \mu_b = \frac{256\mu\nu^2 g_0}{5\pi}; \quad \lambda = \frac{75M(T/\pi)^{1/2}}{8\eta(41-33\eta)\,d^2},$$

where M and d are the mass and diameter of a particle, respectively. For g_0 we adopt the form used by Johnson & Jackson (1987), namely

$$g_0(\nu) = \frac{1}{1-(\nu/\nu_m)^{1/3}},$$

where ν_m denotes the solids volume fraction at closest random packing, taken to be 0.65.

Boundary conditions at the walls, which take account of momentum and energy transfer between the walls and the flowing material, are the same as those used by Wang *et al.* (1996):

$$\boldsymbol{t \cdot \sigma \cdot n} + \left(\frac{\pi\sqrt{3}}{6\nu_m}\right)\phi'\rho_p \nu g_0 T^{1/2} u_{sl} = 0 \tag{7}$$

and

$$\boldsymbol{n \cdot q} = \left(\frac{\pi\sqrt{3}}{6\nu_m}\right)\phi'\rho_p \nu g_0 T^{1/2} u_{sl}^2 - \left(\frac{\pi\sqrt{3}}{4\nu_m}\right)(1-e_w^2)\rho_p \nu g_0 T^{3/2}. \tag{8}$$

In (7) and (8) $\boldsymbol{n}$ is the unit normal to the wall, pointing into the granular material, u_{sl} is the velocity of the granular material in contact with the wall, and $\boldsymbol{t}$ is a unit vector tangent to the wall, in the direction of the slip velocity. The nature of the wall is characterized by ϕ', a 'specularity factor' (which measures the fraction of the momentum of an incident particle in the direction of slip which is transmitted, on average, to the wall in a collision) and e_w, the coefficient of restitution for collisions between particles and the wall.

We now restrict attention to the geometry of figure 1 and to motions confined to the (x, y)-plane. Dimensionless variables are defined as follows:

$$(u^*, v^*) = (u, v)/(g\Delta)^{1/2}; \quad T^* = \rho_p T/N; \quad (X, Y) = (x, y)/\Delta; \quad \tau = t(g/\Delta)^{1/2}, \tag{9}$$

where u and v are the x and y components of velocity, and the equations of motion can then be written as

$$\frac{\partial \nu}{\partial \tau} + \frac{\partial(\nu u^*)}{\partial X} + \frac{\partial(\nu v^*)}{\partial Y} = 0, \tag{10}$$

$$A^2\nu\left[\frac{\partial u^*}{\partial \tau} + u^*\frac{\partial u^*}{\partial X} + v^*\frac{\partial u^*}{\partial Y}\right] = A^2\nu - \frac{\partial(f_1 T^*)}{\partial X} + \frac{\partial}{\partial Y}\left[f_2 ACT^{*1/2}\left(\frac{\partial u^*}{\partial Y} + \frac{\partial v^*}{\partial X}\right)\right]$$
$$+ \frac{\partial}{\partial X}\left[2f_2 ACT^{*1/2}\left(\frac{2}{3}\frac{\partial u^*}{\partial X} - \frac{1}{3}\frac{\partial v^*}{\partial Y}\right)\right] + \frac{\partial}{\partial X}\left[\frac{8\nu^2}{3\pi^{1/2}}\eta g_0 ACT^{*1/2}\left(\frac{\partial u^*}{\partial X} + \frac{\partial v^*}{\partial Y}\right)\right], \tag{11}$$

$$A^2\nu\left[\frac{\partial v^*}{\partial \tau} + u^*\frac{\partial v^*}{\partial X} + v^*\frac{\partial v^*}{\partial Y}\right] = -\frac{\partial(f_1 T^*)}{\partial Y} + \frac{\partial}{\partial X}\left[f_2 ACT^{*1/2}\left(\frac{\partial u^*}{\partial Y} + \frac{\partial v^*}{\partial X}\right)\right]$$
$$+ \frac{\partial}{\partial Y}\left[2f_2 ACT^{*1/2}\left(\frac{2}{3}\frac{\partial v^*}{\partial Y} - \frac{1}{3}\frac{\partial u^*}{\partial X}\right)\right] + \frac{\partial}{\partial Y}\left[\frac{8\nu^2}{3\pi^{1/2}}\eta g_0 ACT^{*1/2}\left(\frac{\partial u^*}{\partial X} + \frac{\partial v^*}{\partial Y}\right)\right], \tag{12}$$

$$f_1(\nu) = \nu[1+4\eta\nu g_0(\nu)]$$

$$f_2(\nu) = \frac{(2+\alpha)\,5\pi^{1/2}}{288\eta(2-\eta)}\left(\frac{1}{g_0(\nu)}+\frac{8}{5}\eta\nu\right)\left[1+\frac{8}{5}\eta(3\eta-2)\,\nu g_0(\nu)\right]+\frac{8\eta\nu^2 g_0(\nu)\,(2+\alpha)}{15\pi^{1/2}}$$

$$f_3(\nu) = \frac{25\pi^{1/2}}{16\eta(41-33\eta)}\left\{\left(\frac{1}{g_0(\nu)}+\frac{12}{5}\eta\nu\right)\left[1+\frac{12}{5}\eta^2(4\eta-3)\,\nu g_0(\nu)\right]+\frac{64}{25\pi}(41-33\eta)\,\eta^2\nu^2 g_0(\nu)\right\},$$

$$f_4(\nu) = \frac{25\pi^{1/2}}{16\eta(41-33\eta)}\left(\frac{1}{\nu g_0(\nu)}+\frac{12}{5}\eta\right)\frac{12}{5}\eta(2\eta-1)(\eta-1)\frac{\mathrm{d}}{\mathrm{d}\nu}[\nu^2 g_0(\nu)],$$

$$f_5(\nu) = \frac{48}{\pi^{1/2}}\eta(1-\eta)\,\nu^2 g_0(\nu), \quad f_6(\nu) = \frac{\pi\sqrt{3}\,\nu g_0(\nu)}{4\nu_m f_3(\nu)}$$

$$f_7(\nu) = \frac{\pi\nu g_0(\nu)}{2\sqrt{3}\nu_m f_3(\nu)}, \quad f_8(\nu) = \frac{\pi\nu g_0(\nu)}{2\sqrt{3}\nu_m f_2(\nu)}$$

TABLE 1. Dimensionless functions

$$\frac{3A\nu}{2C}\left[\frac{\partial T^*}{\partial\tau}+u^*\frac{\partial T^*}{\partial X}+v^*\frac{\partial T^*}{\partial Y}\right] = \frac{\partial}{\partial X}\left[f_3\,T^{*1/2}\frac{\partial T^*}{\partial X}+f_4\,T^{*3/2}\frac{\partial\nu}{\partial X}\right]$$
$$+\frac{\partial}{\partial Y}\left[f_3\,T^{*1/2}\frac{\partial T^*}{\partial Y}+f_4\,T^{*3/2}\frac{\partial\nu}{\partial Y}\right]-\frac{f_5\,T^{*3/2}}{\mathrm{C}^2}+\frac{\mathrm{A}}{\mathrm{C}}\left\{-f_1\,T^*\left(\frac{\partial u^*}{\partial X}+\frac{\partial v^*}{\partial Y}\right)+f_2\,ACT^{*1/2}\right.$$
$$\left.\times\left[\left(\frac{\partial u^*}{\partial Y}+\frac{\partial v^*}{\partial X}\right)^2+\frac{4}{3}\left(\left(\frac{\partial u^*}{\partial X}\right)^2-\left(\frac{\partial u^*}{\partial X}\right)\left(\frac{\partial v^*}{\partial Y}\right)+\left(\frac{\partial v^*}{\partial Y}\right)^2\right)\right]\right\}$$
$$+\frac{8\nu^2}{3\pi^{1/2}}\eta g_0\,A^2T^{*1/2}\left(\frac{\partial u^*}{\partial X}+\frac{\partial v^*}{\partial Y}\right)^2. \tag{13}$$

Here (10) is the continuity equation, (11) and (12) are the two components of momentum balance, (13) is the balance of pseudo-thermal energy, and A and C are two dimensionless parameters defined by

$$A = (g\Delta\rho_p/N)^{1/2}; \quad C = d/\Delta \tag{14a, b}$$

The boundary conditions at the walls of the channel are

$$\frac{\mathrm{d}u^*}{\mathrm{d}Y} = \frac{\phi' f_8\,u^*}{C}, \tag{15}$$

$$\frac{\mathrm{d}T^*}{\mathrm{d}Y} = -T^*\frac{f_4}{f_3}\frac{\mathrm{d}\nu}{\mathrm{d}Y}+\frac{(1-e_w^2)f_6\,T^*}{C}-\frac{\phi' A^2 f_7\,u^{*2}}{C}, \tag{16}$$

where $Y = -0.5$, and

$$\frac{\mathrm{d}u^*}{\mathrm{d}Y} = -\frac{\phi' f_8\,u^*}{C}, \tag{17}$$

$$\frac{\mathrm{d}T^*}{\mathrm{d}Y} = -T^*\frac{f_4}{f_3}\frac{\mathrm{d}\nu}{\mathrm{d}Y}-\frac{(1-e_w^2)f_6\,T^*}{C}+\frac{\phi' A^2 f_7\,u^{*2}}{C}, \tag{18}$$

where $Y = 0.5$. In equations (10)–(18) the symbols f_1–f_8 denote dimensionless functions of ν defined in table 1.

The base state, whose stability will be investigated, is a steady fully developed flow in the x-direction. For such a flow the continuity equation is satisfied trivially, and equations (11), (12) and (13) simplify to

$$\frac{\mathrm{d}}{\mathrm{d}Y}\left[f_2\, ACT^{*1/2}\frac{\mathrm{d}u^*}{\mathrm{d}Y}\right]+A^2\nu=0, \tag{19}$$

$$\frac{\mathrm{d}}{\mathrm{d}Y}[f_1\, T^*]=0, \tag{20}$$

$$\frac{\mathrm{d}}{\mathrm{d}Y}\left[f_3\, T^{*1/2}\frac{\mathrm{d}T^*}{\mathrm{d}Y}+f_4\, T^{*3/2}\frac{\mathrm{d}\nu}{\mathrm{d}Y}\right]+A^2 f_2\, T^{*1/2}\left(\frac{\mathrm{d}u^*}{\mathrm{d}Y}\right)^2-\frac{f_5\, T^{*3/2}}{C^2}=0. \tag{21}$$

The boundary conditions retain the form (15)–(18).

For the base-state flow it is convenient to define a cross-sectional average volume fraction $\bar{\nu}$ and an average dimensionless velocity $\bar{u}^*$ by

$$\bar{\nu}=\int_{-0.5}^{0.5}\nu\,\mathrm{d}Y, \quad \bar{u}^*=\frac{1}{\bar{\nu}}\int_{-0.5}^{0.5}\nu u^*\,\mathrm{d}Y. \tag{22a, b}$$

The second integral above, equal to $\bar{\nu}\,\bar{u}^*$, is a dimensionless measure of the volume flux of solid material down the channel.

3. Steady fully developed flow

For this case the governing equations are (19)–(21), together with the boundary conditions (15)–(18), and some general properties of the solution can be deduced by inspection. Apart from physical properties of the particles and the walls, characterized by ϕ', e_w and e_p (which enters through the factor η in the functions f_1–f_8), the equations contain only two parameters, namely A and C. These determine the solution completely, and hence the value of $\bar{\nu}$, as given by (22a). Thus A and B may be replaced by $\bar{\nu}$ and $\Delta/d(=1/C)$ as the pair of parameters determining the solution. The dimensionless equations (10)–(13), which describe general time-dependent motions, contain no parameters other than A and C, so their solutions are also determined by the values of $\bar{\nu}$ and Δ/d. Since A is determined by these parameters it also follows from (14a) that $N\propto\Delta$.

Solutions of the equations for steady fully developed flow were generated numerically using the finite difference procedure described by Johnson & Jackson (1987), with values for the material properties specified in table 2, and some results are shown in figures 2, 3 and 4. Each figure shows dimensionless temperature, velocity and solids fraction profiles, for two different conditions at the bounding walls. Two sets of curves correspond to boundary conditions of the form (15)–(18), with $e_w=0.5$ and $e_w=0.97$, respectively.

In each case the most striking feature is the presence of a core of relatively high density centred at the middle of the channel. As can be seen by comparing figures 2 and 4, as the width of the channel is increased, the fraction of the width occupied by the dense core does not change significantly, but the density within the core is markedly increased. This is a general feature, as confirmed by computations over a wide range of channel widths. Increasing the mean volume fraction of solids from 0.15 to 0.4 has the effect of increasing the density all across the channel, of course, and in figure 3 it is seen that the density at the centre of the channel approaches 0.6, quite close to the maximum permissible value. This figure also shows that the velocity profile is flattened across the

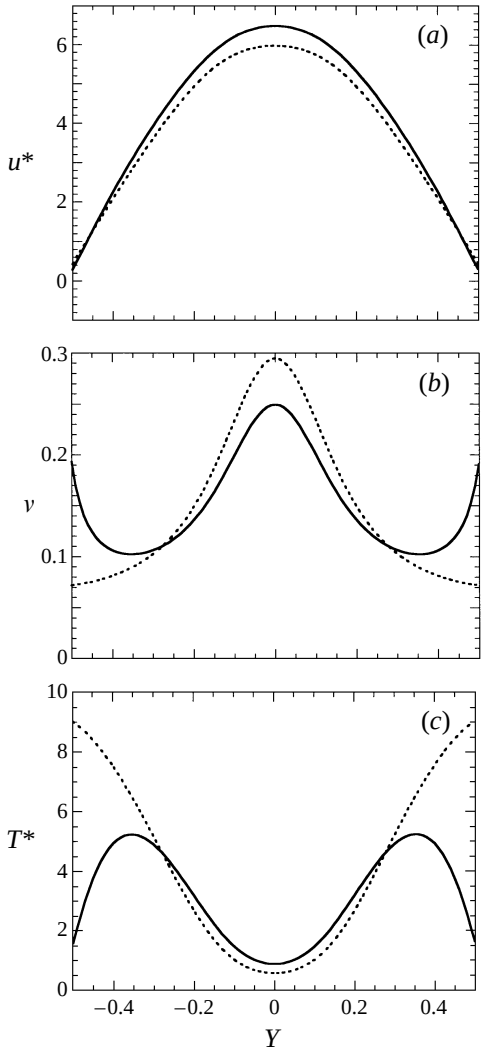

FIGURE 2. Fully developed motion with two wall conditions. Parameter values as in table 2 with $e_w = 0.5$ (sink wall, solid curve) and $e_w = 0.97$ (source wall, dotted curve). $(\bar{\nu}, \Delta/d) = (0.15, 33.3)$.

Particle diameter, d:	0.0018 m
Solid material density, ρ_p:	2980 kg m^{-3}
Particle–particle coefficient of restitution, e_p:	0.95
Specularity coefficient for wall collisions, ϕ':	0.6
Parameter, α:	1.6

TABLE 2. Material properties

region of high density, which is therefore beginning to behave as a plug of material near dense packing, which deforms little as it moves. In each case the granular temperature has a minimum at the point of highest density on the centreline, as might be expected. Changing the nature of the boundary condition at the walls has only a minor effect on the solution in this core region, but a marked influence on the solids fraction and

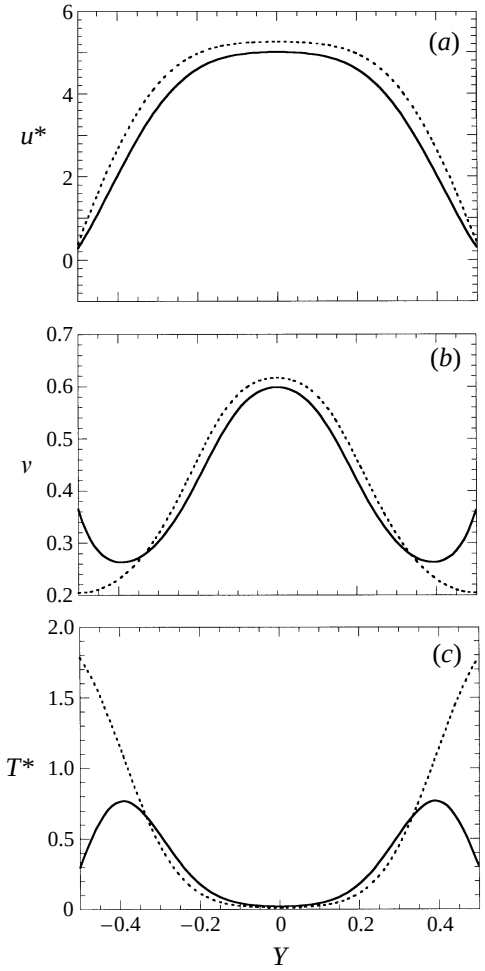

FIGURE 3. As figure 2 but for $(\bar{\nu}, \Delta/d) = (0.40, 33.3)$.

granular temperature profile near the walls. With $e_w = 0.97$, when the walls act as sources of pseudo-thermal energy, the temperature decreases on moving away from the wall and, correspondingly, the solids volume fraction increases. When $e_w = 0.5$, on the other hand, when the walls act as sinks for pseudo-thermal energy, the temperature initially increases on moving away from the walls, while the solids volume fraction decreases. With sink walls, therefore, the central maximum in density is flanked by two minima and, correspondingly, the central minimum in temperature is flanked by two maxima. The core of increased density at the centre of the channel was also seen by Nunziato & Passman (1980) and by Babić (1993*b*), but neither of these authors studied walls which act as sinks for pseudo-thermal energy, so they did not observe the behaviour just described.

Since the values of $\bar{\nu}$ and Δ/d determine the steady solution they also determine both the flux and the mean velocity of solids, as defined in (22), and these quantities are shown in Figure 5. Both increase as the channel width is increased, as would be expected. For each value of the channel width, on the other hand, there exists a value of $\bar{\nu}$ that maximizes the mean velocity and a second, larger value of $\bar{\nu}$ that maximizes the solids flux.

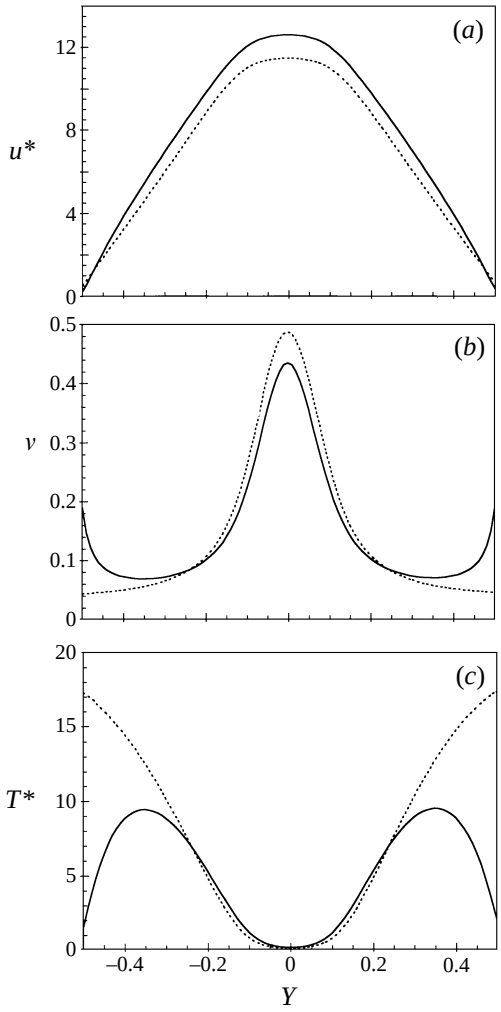

FIGURE 4. As figure 2 but for $(\bar{\nu}, \Delta/d) = (0.15, 66)$.

4. Stability of the fully developed flows

The stability of the fully developed flows is investigated by introducing small perturbations of the form

$$u^* = u_0(Y) + u' \quad \text{where} \quad u' = u_e(Y)\exp(\Omega\tau)\exp(\mathrm{i}K_x X), \tag{23a}$$

$$v^* = v' = v_e(Y)\exp(\Omega\tau)\exp(\mathrm{i}K_x X), \tag{23b}$$

$$\nu = \nu_0(Y) + \nu' \quad \text{where} \quad \nu' = \nu_e(Y)\exp(\Omega\tau)\exp(\mathrm{i}K_x X), \tag{23c}$$

$$T^* = T_0(Y) + T' \quad \text{where} \quad T' = T_e(Y)\exp(\Omega\tau)\exp(\mathrm{i}K_x X), \tag{23d}$$

and linearizing the equations of motion (10)–(13) and the boundary conditions (15)–(18) in these perturbations. The procedure is entirely conventional, as described in Wang *et al.* (1996). The result is a set of ordinary differential equations in the variables u_e, v_e, ν_e and T_e, subject to two-point boundary conditions, constituting an eigenvalue problem for Ω. This is converted to a matrix eigenvalue problem by taking

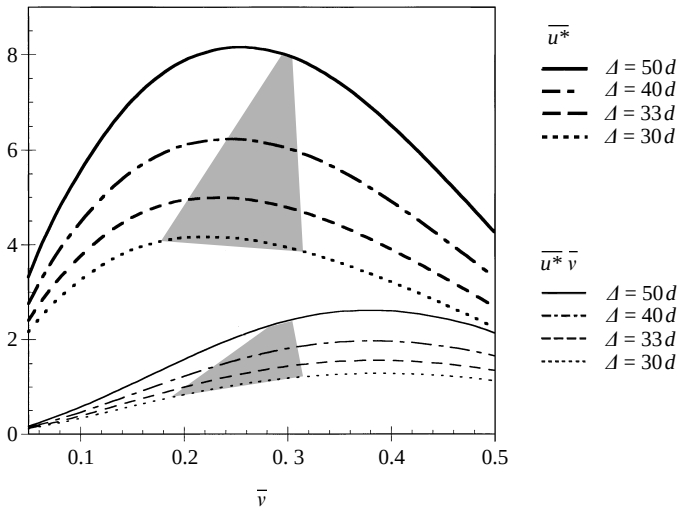

FIGURE 5. Dimensionless mean velocity $\overline{u}^*$ and dimensionless volume flux $\overline{\nu}\,\overline{u}^*$ as functions of mean volume fraction of solids and dimensionless channel width. Parameter values as in table 2. The flow is stable in the shaded domains.

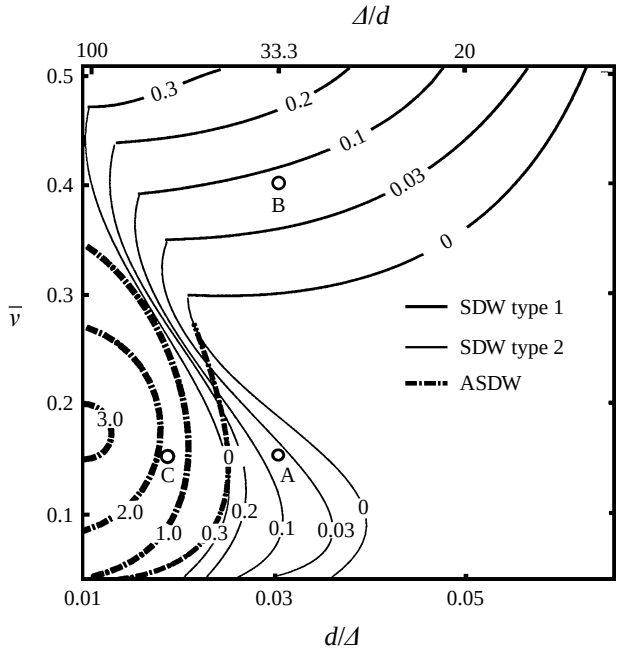

FIGURE 6. Contour map of the dimensionless growth rate Ω_r for the least-stable modes in the $(\overline{\nu}, d/\Delta)$-plane. Parameter values as in table 2, with $e_w = 0.5$. (SDW = symmetric density waves, ASDW = asymmetric density waves.)

finite differences, and the resulting eigenvalues are computed for a sequence of values of K_x to generate a dispersion relation for each set of values of the physical parameters of the problem. The eigenvalue with the largest real part, for all values of K_x and all branches of eigenvalues, is then said to define the *dominant mode* for the given values

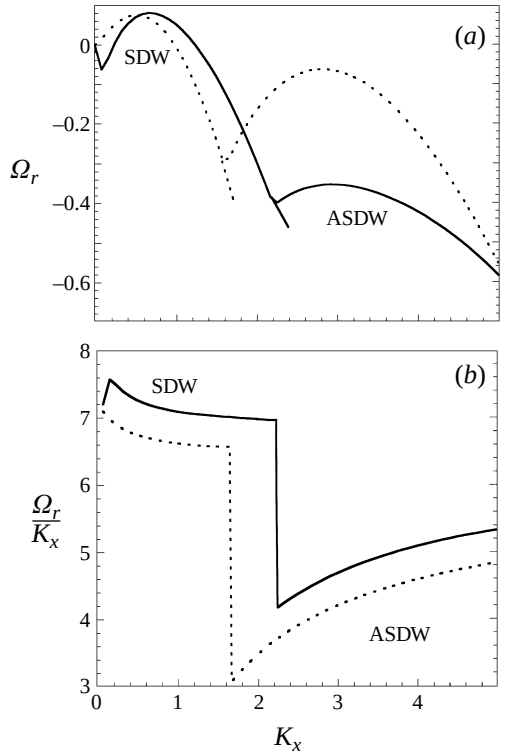

FIGURE 7. Dispersion relations for the least stable modes at $(\bar{\nu}, \Delta/d) = (0.15, 33.3)$. Parameter values as in table 2 and $e_w = 0.5$ (solid curve), $e_w = 0.97$ (dotted curve). (*a*) Dimensionless growth rate. (*b*) Dimensionless velocity of propagation.

of the physical parameters. For these parameter values the fully developed flow is classified as stable or unstable depending on the sign of the real part of the eigenvalue for the dominant mode.

Since the full equations of motion (10)–(13) introduce no new parameters, in addition to $\bar{\nu}$ and Δ/d, the results of the stability computations can be presented as a contour map of the real part of the dominant eigenvalue in the $(\bar{\nu}, d/\Delta)$-plane. Figure 6 shows such a map for a system with the parameter values in table 2, and with $e_w = 0.5$, when the walls act as energy sinks. Each contour is labelled with the corresponding value of Ω_r, and no contours are shown in the region of stability where this is negative. At each value of $\bar{\nu}$ it is seen that the flow is stable for small channel width, but becomes unstable when the width is increased. The range of stability extends farthest when $\bar{\nu} \approx 0.3$. The contours shown clearly belong to three different branches of eigenvalues, which dominate in different parts of the plane. Segments from two of these branches form contours with values of Ω_r between zero and 0.3, while eigenvalues from a third branch, indicated by the heaviest lines, have values of Ω_r which extend as high as 3.0. This branch is dominant for wide channels with low to moderate values of the solids concentration.

We will now examine the dispersion relations and the nature of the eigenfunctions at the three points of the $(\bar{\nu}, d/\Delta)$-plane labelled A, B and C in figure 6. These are located so that their dominant eigenvalues belong to each of the three separate branches identified above. Figure 7 (continuous lines) shows the dimensionless growth rate and the dimensionless velocity of propagation, as functions of K_x, for the least-

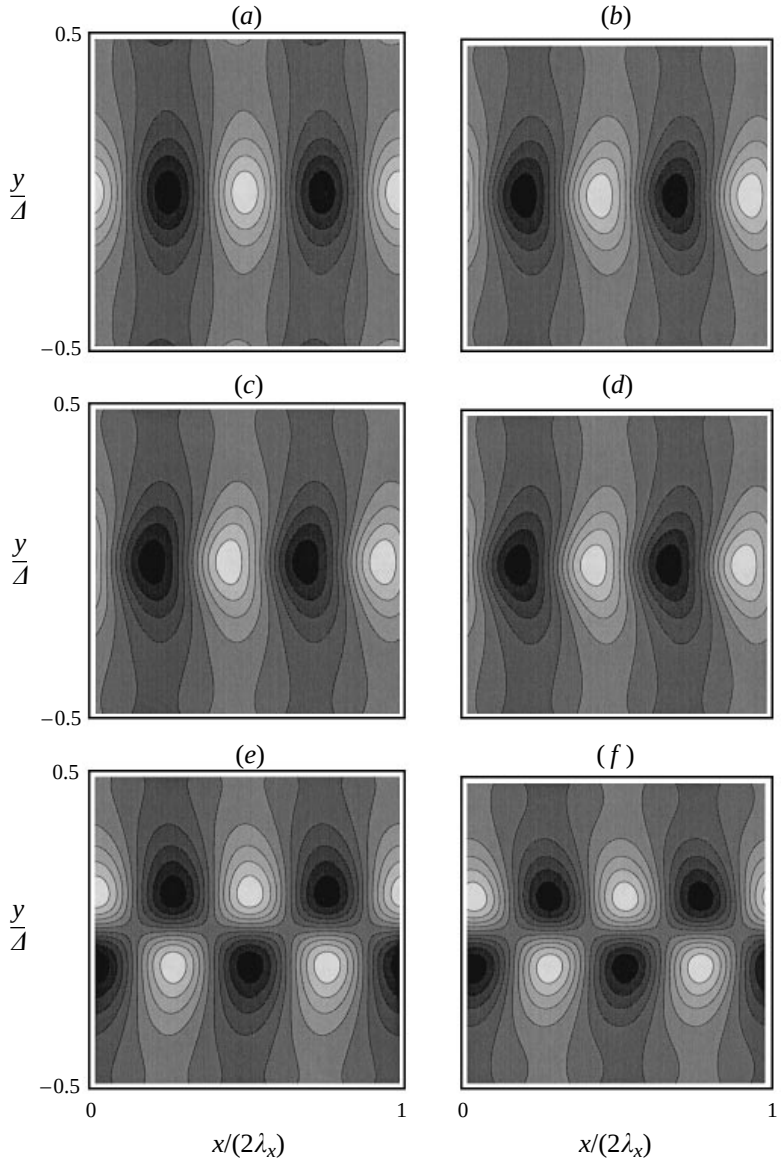

FIGURE 8. Eigenfunctions of the particle concentration for the least-stable mode at various values of K_x, with $(\bar{\nu}, \Delta/d) = (0.15, 33.3)$. Parameter values as for figure 6. (*a*) $K_x = 0.1$, (*b*) $K_x = 1.5$, (*c*) $K_x = 2.0$, (*d*) $K_x = 2.2$, (*e*) $K_x = 2.4$, (*f*) $K_x = 3.5$.

stable branches of eigenvalues at point A, where $(\bar{\nu}, \Delta/d) = (0.15, 33.3)$. The least-stable eigenvalue clearly switches branches at $K_x \approx 2.2$, since two smooth curves for Ω_r cross there and there is a step change in the velocity. (Closer examination of the apparent kinks in the curves near $K_x = 0.2$ reveals that there is actually a smooth minimum in Ω_r and a smooth maximum in the velocity there, with no switch between branches of eigenvalues.) The broken lines in figure 7 are the dispersion relation obtained when the value of e_w is changed to 0.97, so that the walls act as sources of pseudo-thermal energy. Once again there are two branches which, though displaced, clearly correspond to the branches found with the sink walls. Returning to $e_w = 0.5$,

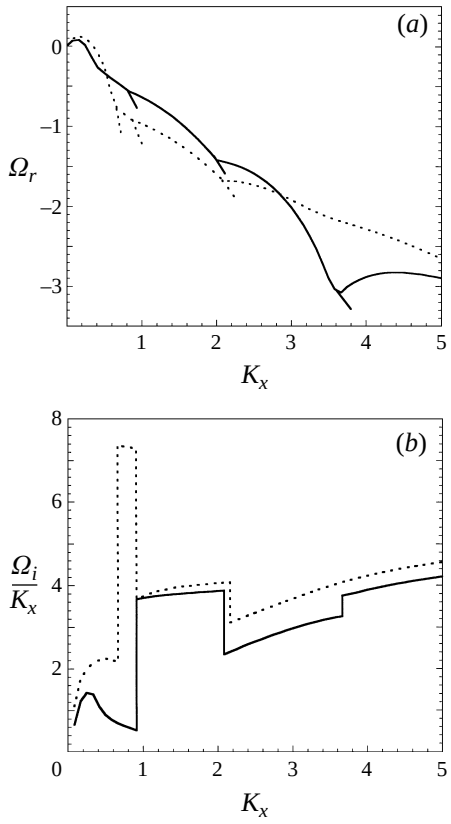

FIGURE 9. Dispersion relations for the least stable modes at $(\bar{\nu}, \Delta/d) = (0.40, 33.3)$. Parameter values as in table 2 and $e_w = 0.5$ (solid curve), $e_w = 0.97$ (dotted curve). (*a*) Dimensionless growth rate. (*b*) Dimensionless velocity of propagation.

figure 8 shows eigenfunctions for the volume fraction of solids as contour plots in the (x, y)-plane, with the darker shading representing denser material. These are presented for a sequence of values of K_x, as specified in the caption, and the physical nature of the perturbations is seen by imagining each pattern to move in the x-direction with the corresponding eigenvelocity. For $K_x \leqslant 2.2$ the patterns are symmetric about the centreline of the channel but for larger values of K_x, when the largest eigenvalue has shifted to a different branch, the patterns become antisymmetric. At this point of the $(\bar{\nu}, \Delta/d)$-plane the dominant eigenvalue belongs to the branch of symmetric density eigenfunctions, and is found at $K_x \approx 0.8$, where the dimensionless velocity of propagation is seen to be approximately 7. Reference to figure 2 shows that the dimensionless velocity of the material in the unperturbed steady state is approximately 6.5 on the centreline of the channel. Thus, the prominent regions of alternating high and low density, which are found along the centreline, move with a speed comparable to, but slightly greater than that of the material at their location. This is in complete contrast with the instabilities of plane Couette flow previously reported by the present authors (Wang *et al.* 1996), which generated density patterns fixed in space.

The dispersion relations at point B of figure 6, where $(\bar{\nu}, \Delta/d) = (0.4,\ 33.3)$, are shown in figure 9, with continuous lines once again corresponding to $e_w = 0.5$ and broken lines to $e_w = 0.97$. There are now switches between four different branches of eigenvalues, as indicated most clearly by jumps in the velocity of propagation. With

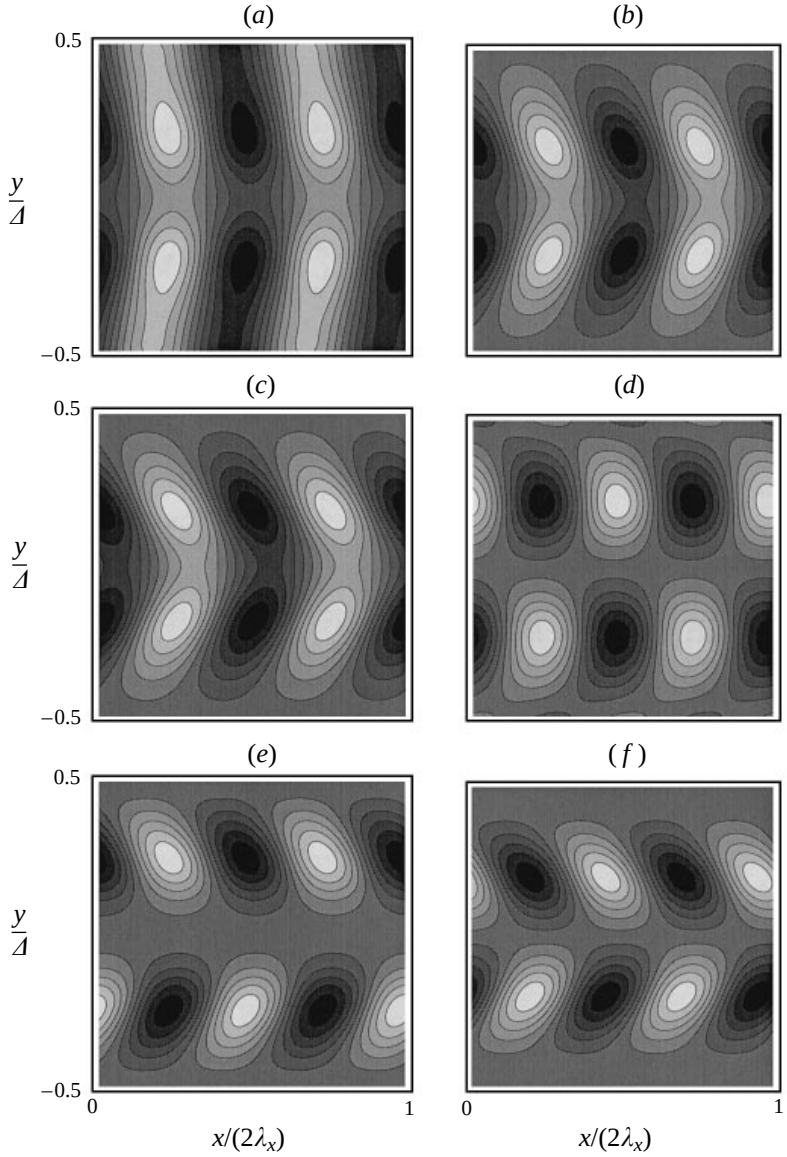

FIGURE 10. Eigenfunctions of the particle concentration for the least-stable mode at various values of K_x, with $(\bar{\nu}, \Delta/d) = (0.40, 33.3)$. Parameter values as for figure 6. (*a*) $K_x = 0.2$, (*b*) $K_x = 1.5$, (*c*) $K_x = 2.0$, (*d*) $K_x = 2.2$, (*e*) $K_x = 3.5$, (*f*) $K_x = 4.0$.

$e_w = 0.5$ eigenfunctions for the volume fraction at a sequence of values of K_x are shown in figure 10. The dominant mode occurs at $K_x \approx 0.2$ and the corresponding eigenfunction appears in panel (*a*). It is again symmetric about the centreline, but differs from the patterns of figure 8 in that there are two rows of regions of alternating high and low density, displaced equally on each side of the centreline. Figure 10(*b*, *c*) shows density eigenfunctions from the second branch of eigenvalues encountered in the dispersion relation. Once again these are symmetric about the centreline and consist of two rows of regions of alternating high and low density. Figures 10(*c*) and 10(*d*) show the eigenfunction just before the switch to the third branch of eigenvalues and just

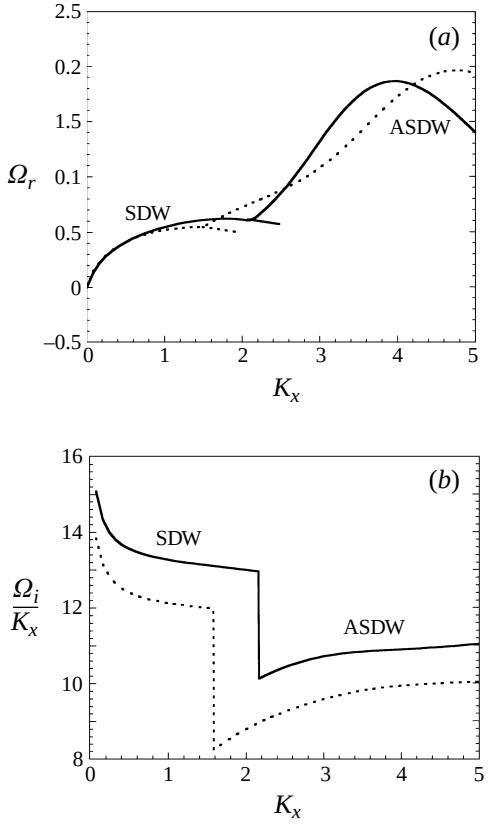

FIGURE 11. Dispersion relations for the least stable modes at $(\bar{\nu}, \Delta/d) = (0.15, 66)$. Parameter values as in table 2 and $e_w = 0.5$ (solid curve), $e_w = 0.97$ (dotted curve). (*a*) Dimensionless growth rate. (*b*) Dimensionless velocity of propagation.

after, respectively. It is seen that there is a significant change in the nature of the density pattern. On the third branch (figure 10*d*, *e*) the pattern is antisymmetric about the centreline. As before there are rows of alternating regions of high and low density disposed on each side of the centreline, but now the regions of high density in one row face the regions of low density in the other. Finally, figure 10(*f*) shows an eigenfunction from the fourth branch of eigenvalues and, once again, this pattern is antisymmetric, closely resembling that in figure 10(*e*). The dominant mode at this location in the $(\bar{\nu}, \Delta/d)$-plane, which is found at $K_x \approx 0.2$, is of the symmetric type and its dimensionless speed of propagation is 1.4. The regions of high and low density are centred at $Y = \pm 0.2$, where figure 3 shows that the dimensionless speed of the granular material in the unperturbed state is 4.4. Thus, in this case, the regions of high and low density move at only about one third of the speed of the granular material in their neighbourhood.

The dispersion relations for point C, where $(\bar{\nu}, \Delta/d) = (0.15, 66)$, are shown in figure 11, and with $e_w = 0.5$ it is seen that the eigenvalue with largest growth rate switches branches only once, at $K_x \approx 2.2$. Eigenfunctions of the density perturbations are displayed in figure 12 for four values of K_x, two from each branch of eigenvalues. For $K_x < 2.2$ these are symmetric about the centreline, while for larger values of K_x they are antisymmetric and the dominant eigenvalue, at $K_x = 3.8$, belongs to the antisymmetric density pattern shown in figure 12(*d*). The dimensionless growth rate of

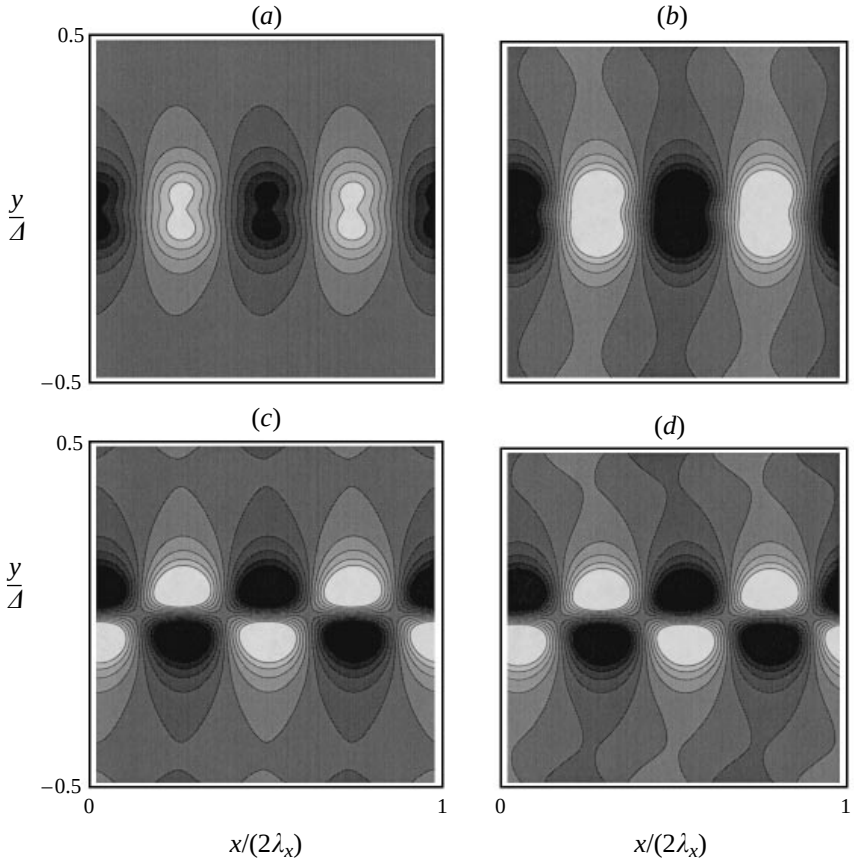

FIGURE 12. Eigenfunctions of the particle concentration of the least-stable mode at various values of K_x, with $(\bar{\nu}, \Delta/d) = (0.15, 66)$. Parameter values as for figure 6. (*a*) $K_x = 0.8$, (*b*) $K_x = 2.0$, (*c*) $K_x = 2.2$, (*d*) $K_x = 3.8$.

this mode is approximately 1.9, much larger than the growth rates of the dominant modes at points A and B of the $(\bar{\nu}, \Delta/d)$-plane. Its dimensionless speed of propagation is 10.8, much larger than that of the dominant mode at point B and larger than, but comparable with, the speed of the dominant mode at point A. The two rows of regions of alternating high and low density are centred roughly at $Y = \pm 0.05$, and reference to figure 4 shows that the dimensionless speed of the granular material in the base state, at this location, is 12.2. Thus, the most prominent density variations move with a speed only a little less than that of the granular material in their neighbourhood.

Note that the coordinates are scaled in different ways for the ordinate and the abscissa in figures 8, 10 and 12. The coordinate y, measuring distance across the channel, is scaled by the channel width, while the x-coordinate is scaled by twice the wavelength of the perturbation. To yield an x-coordinate scaled in the same way as y we have

$$\frac{x}{\Delta} = \frac{x}{2\lambda_x}\left(\frac{4\pi}{K_x}\right).$$

The factor in brackets takes the values 15.7, 62.8 and 3.3 at points A, B and C, respectively, so the dominant modes at points A and B have wavelengths much longer than the channel width, while the wavelength of the strongly unstable dominant mode at point C is comparable with the channel width.

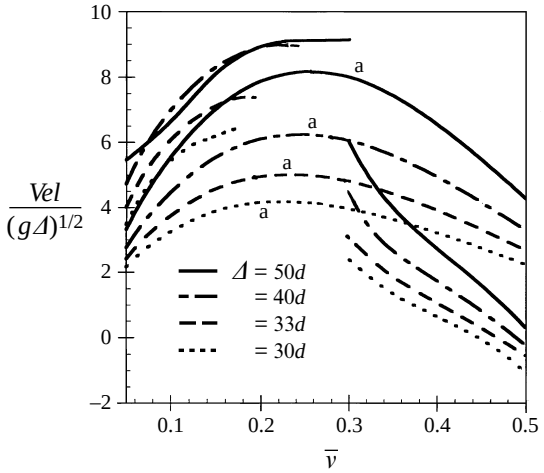

FIGURE 13. Dimensionless propagation velocity of the dominant eigenmode as a function of $\bar{\nu}$ and Δ/d. Parameters as for figure 6. Curves are shown only over intervals of $\bar{\nu}$ and Δ/d for which the system is unstable. Curves labelled 'a' show the dimensionless mean velocity of the particles for comparison.

The dimensionless speed of propagation of the dominant mode is exhibited as a function of $\bar{\nu}$, for four different values of Δ/d, in figure 13. Also shown are curves representing the mean velocity $\bar{u}^*$ in the base state, and from these it is clear that the dominant modes move rather faster than the mean speed of the material when $\bar{\nu} < 0.3$ and slower when $\bar{\nu} > 0.3$. Indeed, for the largest values of $\bar{\nu}$ and smaller channel widths, the instability waves actually move up the channel, counter to the flow of material.

The dimensionless average speed of the descending granular material in the channel is a function of $\bar{\nu}$ and Δ only, so the dimensional average speed is proportional to $g^{1/2}$, where g is the specific gravity force. Thus, for given values of the channel width and the mean concentration of the granular material, its average speed could be controlled if g were adjustable. Nevertheless, as we have seen, the stability boundary is a relation between $\bar{\nu}$ and Δ, unaffected by such changes in the value of g and the resulting changes in the flow rate of the granular material. Furthermore, in the unstable region both the dimensionless growth rate of the dominant mode and its dimensionless velocity of propagation depend only on $\bar{\nu}$ and Δ, so the dimensional growth rate and dimensional velocity are both proportional to $g^{1/2}$. Thus, with given channel width and particle concentration, if the flow rate is varied by changing the value of g, both the growth rate of the dominant disturbance and its speed of propagation will be found to vary in proportion to the flow rate. Consequently the growth distance, that is the distance the disturbance travels while growing in amplitude by a factor e, is independent of the flow rate.

Scrutiny of figures 7, 9 and 11 reveals that the pattern of the dispersion relations is not changed when the boundary conditions change; only the positions of the switches between the branches of eigenvalues and the associated jumps in velocity are altered. This insensitivity of qualitative features of behaviour to the nature of the boundary conditions is underlined by figure 14, which compares the density eigenfunctions of the dominant modes at points A, B and C of the $(\bar{\nu}, \Delta/d)$-plane, for boundary conditions with both $e_w = 0.5$ and $e_w = 0.97$. At each point the contour maps for the cases of sink and source walls are almost indistinguishable.

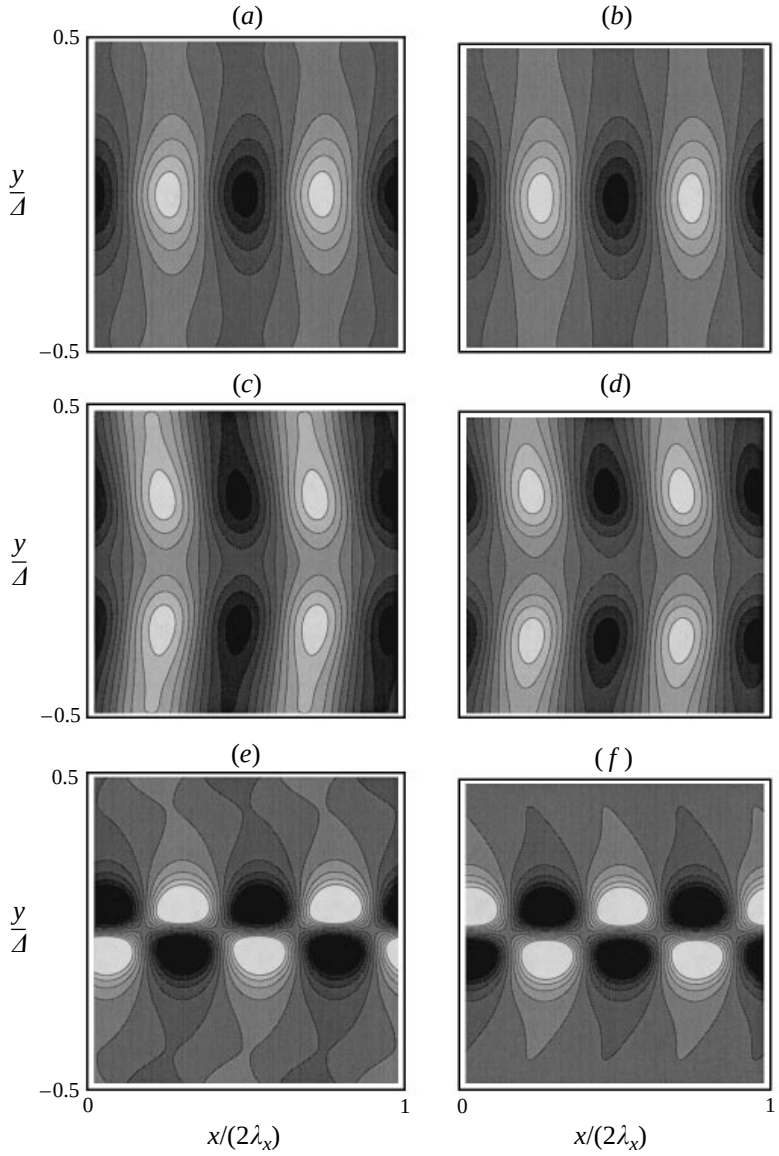

FIGURE 14. Eigenfunctions of the particle concentration for the dominant instability at three points of the $(\bar{\nu}, \Delta/d)$-plane. (*a*) $(\bar{\nu}, \Delta/d) = (0.15, 33.3)$, $e_w = 0.5, K_x = 0.68$; (*b*) $(\bar{\nu}, \Delta/d) = (0.15, 33.3)$, $e_w = 0.97, K_x = 0.52$; (*c*) $(\bar{\nu}, \Delta/d) = (0.4, 33.3)$, $e_w = 0.5, K_x = 0.13$; (*d*) $(\bar{\nu}, \Delta/d) = (0.4, 33.3)$, $e_w = 0.97, K_x = 0.17$; (*e*) $(\bar{\nu}, \Delta/d) = (0.15, 66), e_w = 0.5, K_x = 3.97$; (*f*) $(\bar{\nu}, \Delta/d) = (0.15, 66)$, $e_w = 0.97, K_x = 4.77$.

5. Conclusion

The instabilities reported here share some features of those found by Wang *et al.* (1996) for plane Couette flow, but also differ in important respects. For plane Couette flow two types of unstable mode were found: a rather weak one corresponding to the development of layers of alternating high and low density parallel to the planes of shear, and a stronger mode generating more complicated stationary patterns of density variations. These were referred to as layering modes and stationary modes, respectively. The layering modes are also present in unbounded plane shear flow but the stationary

modes have no analogue in the unbounded case, and therefore owe their existence to the presence of the boundaries. In the system investigated here all the instability modes are associated with the presence of the bounding walls but, as in the case of the stationary modes for plane Couette flow, their behaviour is found to be remarkably insensitive to the physical nature of these walls, represented by the value of e_w. Here, however, the similarity between the two cases ends. In plane Couette flow all the unstable density patterns are at rest in the frame for which the bounding walls have equal and oppositely directed velocities, so the material itself moves through these density patterns. In the present case, on the other hand, all the eigenmodes are travelling waves and, for lower values of the solids volume fraction, they move at speeds comparable with that of the granular material itself. Thus, the clusters of high and low density in these modes convect with speeds comparable to that of the solid material.

The physical mechanism of instability also appears to be different in the two cases. For the layering mode in plane Couette flow we find that the condition of neutral stability is unchanged if the inertial terms are omitted from the momentum balance and the thermal inertia terms from the energy balance. Thus, the onset of this instability is controlled entirely by the inelasticity of collisions between pairs of particles. Nevertheless, the form of the dispersion relation between growth rate and wavenumber, within the domain of instability, is influenced markedly by the presence of inertial terms. In the absence of these terms the growth rate increases monotonically with the spacing between the layers, while in the presence of inertia it passes through a maximum, so that there is a dominant spacing for which the layering pattern grows most rapidly. In contrast, the stationary modes for Couettte flow are inertial in origin; they disappear if the inertial terms are omitted from the equations of motion. The instabilities of vertical channel flow, found in the present paper, also require the presence of the inertial terms; if the left-hand side of equation (2) is multiplied by an adjustable numerical factor, all modes are found to become stable when this is sufficiently small. It is less clear that inelasticity of particle–particle collisions is necessary for instability. Certainly the neutral stability curve in figure 6 moves to the left as the value of e_p is increased, so the domain of stable behaviour becomes larger. Also, when $e_p = 1$, the flow is found to be stable to the smallest values of d/Δ explored directly in our computations. However, it seems likely that unstable behaviour still survives, though for smaller values of d/Δ, since the assembly of particles then degenerates into a classical dense gas, whose flow might be expected to be unstable in a sufficiently wide channel. Unfortunately we cannot offer a detailed qualitative explanation of the physical mechanism responsible for the instabilities. This is, perhaps, not surprising. The mechanism of instability in the well known and much simpler case of channel flow of an incompressible Newtonian fluid is also difficult to visualize.

The system studied becomes more unstable as e_p is decreased so it would be interesting to investigate the behaviour with highly inelastic collisions. However, it should be recalled that the equations of motion used here are derived on the assumption that the coefficient of restitution differs only slightly from unity, so they do not provide an adequate theoretical basis for such a study.

There are two other publications describing phenomena which, on the face of it, might be related to the instabilities found here. Sanders & Ackermann (1991) described 'slug flow' patterns generated in numerical simultations of the flow of an assembly of inelastic circular disks down an inclined channel, and Raafat, Hulin & Herrmann (1996) observed slugging in experiments on the flow of a granular material

down a vertical pipe. The former may be a consequence of the development to high amplitude of the instabilities we have found. However, we would be reluctant to interpret the latter phenomenon in this way since, as is well known, the behaviour of systems of this type is usually dominated by effects associated with interaction between the particles and the interstitial air.

This work has been supported by the National Science Foundation under grants CTS 92-07469 and CTS 94-21661, and by the International Fine Particle Research Institute. C.-H. Wang also acknowledges support by a Charlotte Elizabeth Procter Fellowship during the later stages of the work.

REFERENCES

Babić, M. 1993*a* On the stability of rapid granular flows. *J. Fluid Mech.* **254**, 127–150.

Babić, M. 1993*b* Gravity-driven flows of smooth, inelastic disks between parallel bumpy boundaries. *J. Appl. Mech.* **60**, 59–64.

Goldhirsch, I., Tan, M.-L. & Zanetti, G. 1993 A molecular dynamical study of granular fluids. I: the unforced granular gas in two dimensions. *J. Sci. Comput.* **8**, 1–40.

Hopkins, M. A. & Louge, M. Y. 1991 Inelastic microstructure in rapid granular flows of smooth disks. *Phys. Fluids* A **3**, 47–57.

Johnson, P. C. & Jackson, R. 1987 Frictional-collisional constitutive relations for granular materials, with application to plane shearing. *J. Fluid Mech.* **176**, 67–93.

Lun, C. K. K., Savage, S. B., Jeffrey, D. J. & Chepurniy, N. 1984 Kinetic theories for granular flow: inelastic particles in Couette flow and slightly inelastic particles in a general flow field. *J. Fluid Mech.* **140**, 223–256.

Nunziato, J. W. & Passman, S. L. 1980 Gravitational flows of granular materials with incompressible grains. *J. Rheol.* **24**, 395–420.

Raafat, T., Hulin, J. P. & Herrmann, H. J. 1996 Density waves in dry granular media falling through a vertical pipe. *Phys. Rev.* E **53**, 4345–4349.

Sanders, B. E. & Ackermann, N. L. 1991 Instability in simulated granular chute flows. *J. Engng Mech.* **117**, 2396–2406.

Savage S. B. 1992 Instabilities of unbounded uniform granular shear flow. *J. Fluid Mech.* **241**, 109–123.

Schmid, P. J. & Kytomaa, H. K. 1994 Transient and asymptotic stability of granular shear flow. *J. Fluid Mech.* **264**, 255–275.

Wang, C.-H., Jackson, R. & Sundaresan, S. 1996 Stability of bounded rapid shear flows of a granular material. *J. Fluid Mech.* **308**, 31–62.